Supplemental Material for "In-plane flexoelectricity in two-dimensional D_{3d} crystals"

Matteo Springolo, Miquel Royo and Massimiliano Stengel

October 17, 2023

Contents

1 Introduction

Here we provide additional material in support of our results. In Sec. 2, we prove the absence of a metric contribution to the in-plane coefficients considered here, in contrast to the out-of-plane case studied in our previous work [1]. In Sec. 3, we provide a detailed derivation of the in-plane 2D flexoelectric coefficients in their type-II form. Then, we split the total (relaxed-ion) response into clamped-ion and lattice-mediated contributions, and show its relation with the 3D type-I flexoelectric tensor. In Sec. 4, we provide the detailed computational parameters used in the primitive cell linear-response, while in Sec. 5 we describe the computational method employed for the calculation of the axial polarization within

SnS_2 nanotubes, and discuss the related outcomes. In Sec. 6, we show that the in-plane flexoelectric coefficients also provide an exact description of the longitudinal macroscopic electric fields associated to a flexural phonon. In Sec. 7 the impact of the choice of the exchange-correlation functional on the quantity considered in this work is discussed. Sec. 8 is assigned to the illustration of two experimental setups that could possibly confirm the theoretical predictions and results presented in the main text. Finally, in Sec. 9, the non trivial polarization textures associated with several types of ripples are presented.

2 Flexoelectric response of 2D materials

The flexoelectric response of a quasi-2D material can be either defined as the derivative (with respect to the uniform strain-gradient $\varepsilon_{\beta\gamma,\lambda}$ describing the deformation considered) of the electrostatic potential V at fixed macroscopic displacement field $\mathbf{D}$ (open circuit) or as the derivative of the macroscopic $\mathbf{D}$ at fixed V (short circuit). While the former definition is appropriate for the out-of-plane response [1], the latter is the natural choice for the in-plane components studied here, given the extended nature of the crystal therein. Following the prescriptions of Refs. [2, 3], we define the flexoelectric response via a curvilinear-coordinate representation of the microscopic electric displacement field via

$$\hat{\mathbf{D}}^{(1)}(\mathbf{r}) = \hat{\boldsymbol{\epsilon}}^{(0)} \cdot \hat{\mathbf{E}}^{(1)}(\mathbf{r}) + \hat{\boldsymbol{\epsilon}}^{(1)}(\mathbf{r}) \cdot \hat{\mathbf{E}}^{(0)}(\mathbf{r}) + \hat{\mathbf{P}}^{(1)}(\mathbf{r}). \tag{1}$$

(The hat symbol indicates the curvilinear representation of the relevant quantities and the (1) superscript indicates first order in the strain gradient.) The second term in the rhs of Eq. (1), $\hat{\boldsymbol{\epsilon}}^{(1)}(\mathbf{r}) \cdot \hat{\mathbf{E}}^{(0)}(\mathbf{r})$, orginates from the *geometric* variation of the vacuum permittivity $\hat{\boldsymbol{\epsilon}}(\mathbf{r}) = \epsilon_0 \sqrt{g} \hat{\mathbf{g}}^{-1}(\mathbf{r})$ [3], and couples the linear variation of the curvilinear microscopic electric displacement with the microscopic electric field within the undistorted configuration, $\hat{\mathbf{E}}^{(0)}(\mathbf{r}) = \mathbf{E}^{(0)}(\mathbf{r})$ ($\mathbf{E}^{(0)}(\mathbf{r})$ being the Cartesian representation of the electric field) through the linear variation of the metric tensor $\hat{\mathbf{g}}(\mathbf{r})$ and its determinant g. This means that, in principle, a metric contribution may be present (and hence the first-order $\hat{\mathbf{D}}$ may differ from the first-order $\hat{\mathbf{P}}$) even if short-circuit electrical boundary conditions are assumed. However, one can show that, for the in-plane response considered in this work, the geometric contribution vanishes. Indeed the linear variation of the metric contribution, $\hat{\mathbf{D}}^{(\mathrm{met})} = \hat{\boldsymbol{\epsilon}}^{(1)}(\mathbf{r}) \cdot \hat{\mathbf{E}}^{(0)}(\mathbf{r})$, due to a uniform strain-gradient of the form $\varepsilon_{\beta\gamma,z}$ takes the form [3]

$$\frac{\partial \hat{D}_\alpha^{(\mathrm{met})}(\mathbf{r})}{\partial \varepsilon_{\beta\gamma,z}} = \epsilon_0 z \left(\delta_{\beta\gamma} E_\alpha^{(0)}(\mathbf{r}) - \delta_{\alpha\beta} E_\gamma^{(0)}(\mathbf{r}) - \delta_{\alpha\gamma} E_\beta^{(0)}(\mathbf{r}) \right). \tag{2}$$

and its in-plane components ($\alpha = x$, or y) are zero when integrated on the volume of the unit-cell, leading to

$$\langle \hat{\mathbf{D}}_\parallel^{\mathrm{SC}} \rangle = \langle \hat{\mathbf{D}}_\parallel \rangle |_{\langle \hat{\mathbf{E}}_\parallel^{(1)} \rangle = 0} = \langle \hat{\mathbf{P}}_\parallel^{(1)} \rangle |_{\langle \hat{\mathbf{E}}_\parallel^{(1)} \rangle = 0} \tag{3}$$

once the unit-cell average of the in-plane response is considered and SC conditions ($\langle \hat{\mathbf{E}}_\parallel^{(1)} \rangle = 0$) are applied.

3 In-plane response to a flexural deformation

The microscopic *curvilinear* polarization linear-response along an in-plane (curvilinear) direction ($\alpha = x$ or y) due to a symmetrized uniform strain-gradient of the type $\varepsilon_{\beta\gamma,\lambda}$ can be written as [2, 3]

$$\hat{P}^{(1)}_{\alpha}(\mathbf{r}) = P^{(\mathrm{U})}_{\alpha,\beta\gamma}(\mathbf{r})\varepsilon_{\beta\gamma}(\mathbf{r}) + P^{(\mathrm{G})}_{\alpha\lambda,\beta\gamma}(\mathbf{r})\varepsilon_{\beta\gamma,\lambda} \tag{4}$$

where summation over repeated indices is implied, and

$$P^{(\mathrm{U})}_{\alpha,\beta\gamma}(\mathbf{r}) = \underbrace{-\frac{1}{2}\sum_{k}\left(P^{(1,\gamma)}_{\alpha,\kappa\beta}(\mathbf{r}) + P^{(1,\beta)}_{\alpha,\kappa\gamma}(\mathbf{r})\right)}_{\text{Clamped-Ion}} + \underbrace{P^{(0)}_{\alpha,\kappa\rho}(\mathbf{r})\Gamma^{\kappa}_{\rho,\beta\gamma}}_{\text{Lattice-Mediated}}, \tag{5a}$$

$$\begin{aligned} P^{(\mathrm{G})}_{\alpha\lambda,\beta\gamma}(\mathbf{r}) = &\underbrace{\frac{1}{2}\sum_{\kappa}\left(P^{(2,\gamma\lambda)}_{\alpha,\kappa\beta}(\mathbf{r}) + P^{(2,\lambda\beta)}_{\alpha,\kappa\gamma}(\mathbf{r}) - P^{(2,\beta\gamma)}_{\alpha,\kappa\lambda}(\mathbf{r})\right)}_{\text{Clamped-Ion}} \\ &- \underbrace{P^{(1,\lambda)}_{\alpha,\kappa\rho}(\mathbf{r})\Gamma^{\kappa}_{\rho,\beta\gamma}}_{\text{Mixed}} + \underbrace{P^{(0)}_{\alpha,\kappa\rho}(\mathbf{r})L^{\kappa}_{\rho\lambda,\beta\gamma}}_{\text{Lattice-Mediated}}. \end{aligned} \tag{5b}$$

Here, $\mathbf{P}^{(\mathrm{U})}_{\beta\gamma}(\mathbf{r})$ is the microscopic polarization linear-response due to a uniform symmetrized strain $\varepsilon_{\beta\gamma}$, and $\mathbf{P}^{(\mathrm{U})}_{\beta\gamma}(\mathbf{r})r_{\lambda} = \mathbf{P}^{(\mathrm{U})}_{\beta\gamma}(\mathbf{r})\dfrac{\partial\varepsilon_{\beta\gamma}(\mathbf{r})}{\partial\varepsilon_{\beta\gamma,\lambda}}$ and $\mathbf{P}^{(\mathrm{G})}_{\lambda,\beta\gamma}(\mathbf{r})$ have the physical interpretation of a local piezoelectric (U) and a flexoelectric (G) (type-II) coefficient respectively due to a uniform strain-gradient of the type $\varepsilon_{\beta\gamma,\lambda} = \partial\varepsilon_{\beta\gamma}(\mathbf{r})/\partial r_{\lambda}$. A flexural deformation can be described by a symmetrized transverse strain gradient of the type $\varepsilon_{\beta\gamma,z}$ and then the longitudinal microscopic polarization response due to a flexural deformation is

$$\frac{\partial\hat{P}_{\alpha}(\mathbf{r})}{\partial\varepsilon_{\beta\gamma,z}} = P^{(\mathrm{U})}_{\alpha,\beta\gamma}(\mathbf{r})z + P^{(\mathrm{G})}_{\alpha z,\beta\gamma}(\mathbf{r}). \tag{6}$$

The total (relaxed-ion) 2D longitudinal flexoelectric coefficient is finally obtained as

$$\mu^{\mathrm{2D}}_{\alpha z,\beta\gamma} = \frac{1}{S}\int_{\Omega} d^3r \frac{\partial\hat{P}_{\alpha}(\mathbf{r})}{\partial\varepsilon_{\beta\gamma,z}} = \frac{1}{S}\int_{\Omega} d^3r P^{(\mathrm{U})}_{\alpha,\beta\gamma}(\mathbf{r})z + L\mu^{\mathrm{II}}_{\alpha z,\beta\gamma} \tag{7}$$

where S is the unit-cell surface, L the out-of-plane dimension of the supercell where the layer is accomodated in, and the relation $\mu^{\mathrm{II}}_{\alpha z,\beta\gamma} = \dfrac{1}{\Omega}\int_{\Omega} d^3r P^{(\mathrm{G})}_{\alpha z,\beta\gamma}(\mathbf{r})$ [4, 3] has been used. $\mu^{\mathrm{II}}_{\alpha z,\beta\gamma}$ is the type-II bulk flexoelectric coefficient of the supercell, the volume of the latter indicated as Ω.

In the following sections we shall recast Eq. (7) in a form that is suitable for direct implementation and that provides an exact separation between clamped-ion (CI) and lattice-mediated (LM) contributions.

3.1 Clamped-ion 2D flexocoefficient

The clamped-ion contribution to $\mu^{\mathrm{2D}}_{\alpha z,\beta\gamma}$ is formally written as

$$\mu^{\mathrm{2D,CI}}_{\alpha z,\beta\gamma} = -\frac{1}{2S}\sum_{\kappa}\int_{\Omega} d^3r \left(P^{(1,\gamma)}_{\alpha,\kappa\beta}(\mathbf{r})z + P^{(1,\beta)}_{\alpha,\kappa\gamma}(\mathbf{r})z\right) + L\mu^{\mathrm{II,CI}}_{\alpha z,\beta\gamma}. \tag{8}$$

Using the fact that the system is finite along the out-of-plane z-direction, we can write

$$\begin{aligned}
-\frac{1}{S}\sum_{\kappa}\int_{\Omega} d^3r z P^{(1,\gamma)}_{\alpha,\kappa\beta}(\mathbf{r}) &= -\frac{1}{S}\sum_{\kappa}\int_{\Omega} d^3r \left(z-\tau_{\kappa z}\right) P^{(1,\gamma)}_{\alpha,\kappa\beta}(\mathbf{r}) - \frac{1}{S}\sum_{\kappa}\tau_{\kappa z}\int_{\Omega} d^3r P^{(1,\gamma)}_{\alpha,\kappa\beta}(\mathbf{r}) \\
&= -\frac{1}{S}\sum_{\kappa}\int_{\Omega} d^3r P^{(2,\gamma z)}_{\alpha,\kappa\beta}(\mathbf{r}) - \frac{1}{S}\sum_{\kappa}\tau_{\kappa z}\int_{\Omega} d^3r P^{(1,\gamma)}_{\alpha,\kappa\beta}(\mathbf{r}) \\
&= -2L\mu^{\mathrm{I,CI}}_{\alpha\beta,\gamma z} - L\sum_{\kappa}\tau_{\kappa z}\bar{P}^{(1,\gamma)}_{\alpha,\kappa\beta}.
\end{aligned} \tag{9}$$

Here, the overbar indicates avarage over the supercell volume and we have used the relationship [4] between the type-I CI flexocoefficients and the sublattice summation of $\bar{P}^{(2,\gamma z)}_{\alpha,\kappa\beta}$. Finally, using the relationship $\mu^{\mathrm{I}}_{\alpha\beta,\gamma z} = (1/2)\left(\mu^{\mathrm{II}}_{\alpha z,\beta\gamma} + \mu^{\mathrm{II}}_{\alpha\gamma,\beta z}\right)$ [3, 4] and gathering all the terms together, Eq.(8) can be rewritten as

$$\mu^{\mathrm{2D,CI}}_{\alpha z,\beta\gamma} = -\frac{L}{2}\left[\left(\mu^{\mathrm{II,CI}}_{\alpha\gamma,z\beta} + \mu^{\mathrm{II,CI}}_{\alpha\beta,z\gamma}\right) + \left(\bar{P}^{(1,\beta)}_{\alpha,\kappa\gamma} + \bar{P}^{(1,\gamma)}_{\alpha,\kappa\beta}\right)\tau_{\kappa z}\right]. \tag{10}$$

3.2 Lattice-mediated 2D flexocoefficient

The remaining, no clamped-ion type, contributions to the 2D flexocoefficient of Eq. (7) are

$$\frac{1}{S}\int_{\Omega} d^3r z P^{(0)}_{\alpha,\kappa\rho}(\mathbf{r})\Gamma^{\kappa}_{\rho,\beta\gamma} - L\bar{P}^{(1,z)}_{\alpha,\kappa\rho}\Gamma^{\kappa}_{\rho,\beta\gamma} + \frac{1}{S}Z^{(\alpha)}_{\kappa\rho}L^{\kappa}_{\rho z,\beta\gamma}. \tag{11}$$

The first term, coming from Eq. (5a), can be manipulated likewise its CI counterpart, as follows

$$\begin{aligned}
\frac{1}{S}\int_{\Omega} d^3r z P^{(0)}_{\alpha,\kappa\rho}(\mathbf{r})\Gamma^{\kappa}_{\rho,\beta\gamma} &= \frac{1}{S}\int_{\Omega} d^3r \left(z-\tau_{\kappa z}\right) P^{(0)}_{\alpha,\kappa\rho}(\mathbf{r})\Gamma^{\kappa}_{\rho,\beta\gamma} + \frac{1}{S}\tau_{\kappa z}\int_{\Omega} d^3r P^{(0)}_{\alpha,\kappa\rho}(\mathbf{r})\Gamma^{\kappa}_{\rho,\beta\gamma} \\
&= \frac{1}{S}\int_{\Omega} d^3r P^{(1,z)}_{\alpha,\kappa\rho}(\mathbf{r})\Gamma^{\kappa}_{\rho,\beta\gamma} + \tau_{\kappa z}\frac{1}{S}\int_{\Omega} d^3r P^{(0)}_{\alpha,\kappa\rho}(\mathbf{r})\Gamma^{\kappa}_{\rho,\beta\gamma} \\
&= L\bar{P}^{(1,z)}_{\alpha,\kappa\rho}\Gamma^{\kappa}_{\rho,\beta\gamma} + \frac{1}{S}Z^{(\alpha)}_{\kappa\rho}\tau_{\kappa z}\Gamma^{\kappa}_{\rho,\beta\gamma}.
\end{aligned} \tag{12}$$

Now, after observing that the first term at the rhs exactly cancels the mixed one [second term in Eq. (11)], we are left with a purely lattice-mediated contribution written as

$$\mu^{\mathrm{2D,LM}}_{\alpha z,\beta\gamma} = \frac{1}{S}Z^{(\alpha)}_{\kappa\rho}\mathcal{L}^{\kappa}_{\rho z,\beta\gamma} \tag{13}$$

where $\mathcal{L}^{\kappa}_{\rho z,\beta\gamma}$ is the internal relaxation of the κ-atom in the isolated slab due to the flexural deformation. The last quantity can be likewise split as

$$\mathcal{L}^{\kappa}_{\rho z,\beta\gamma} = \Gamma^{\kappa}_{\rho,\beta\gamma}\tau_{\kappa z} + L^{\kappa}_{\rho z,\beta\gamma}, \tag{14}$$

i.e., in terms of the piezoelectric ($\boldsymbol{\Gamma}$) and flexoelectric ($\boldsymbol{L}$) internal tensors of the 3D supercell.

3.3 Relation to the type-I bulk coefficients

In the main text we claim that the "2D" type-II flexoelectric coefficients defined and calculated in this work directly relate to the macroscopic "3D" type-I flexoelectric coefficients of the supercell. To support this statement, here we shall demonstrate the following relationship

$$\mu^{\mathrm{2D}}_{\alpha z,\beta\gamma} = -L\mu^{\mathrm{I}}_{\alpha z,\beta\gamma}. \tag{15}$$

Regarding the clamped-ion part, notice that, exploiting the relation $\Gamma^{\kappa}_{\alpha,z\beta} = \Gamma^{\kappa}_{\alpha,\beta z} = -\delta_{\alpha\beta}\tau_{\kappa z}$ valid for an isolated slab, Eq.(10) can be recast in the form

$$\mu^{\mathrm{2D,CI}}_{\alpha z,\beta\gamma} = -\frac{1}{2}L\left(\mu^{\mathrm{II,el}}_{\alpha\gamma,z\beta} + \mu^{\mathrm{II,el}}_{\alpha\beta,z\gamma}\right), \tag{16}$$

with $\mu^{\mathrm{II,el}}_{\alpha\gamma,z\beta}$ being the type-II bulk *electronic* flexoelectric tensor defined as in Ref. [5]:

$$\mu^{\mathrm{II,el}}_{\alpha\gamma,z\beta} = \mu^{\mathrm{II,CI}}_{\alpha\gamma,z\beta} - \bar{P}^{(1,\gamma)}_{\alpha,\kappa\rho}\Gamma^{\kappa}_{\rho,z\beta} \tag{17}$$

Regarding the lattice-mediated contribution, notice that in a free-standing layer the shear components of the type-I internal-strain tensor $\mathbf{N}$ [4] and the transverse components of the type-II tensor are related by

$$N^{\kappa}_{\rho z,\beta\gamma} = -\Gamma^{\kappa}_{\rho,\beta\gamma}\tau_{\kappa z} - L^{\kappa}_{\rho z,\beta\gamma} = -\mathcal{L}^{\kappa}_{\rho z,\beta\gamma}. \tag{18}$$

Now, recalling the relationship between the type-I and type-II representations of the flexoelectric tensor [3, 4],

$$\frac{1}{2}\left(\mu^{\mathrm{II}}_{\alpha\gamma,z\beta} + \mu^{\mathrm{II}}_{\alpha\beta,z\gamma}\right) = \mu^{\mathrm{I}}_{\alpha z,\beta\gamma} \tag{19}$$

we can conclude that

$$\mu^{\mathrm{2D,CI}}_{\alpha z,\beta\gamma} = -L\mu^{\mathrm{I,el}}_{\alpha z,\beta\gamma}, \qquad \mu^{\mathrm{2D,LM}}_{\alpha z,\beta\gamma} = -L\mu^{\mathrm{I,LM}}_{\alpha z,\beta\gamma}, \tag{20}$$

which proves Eq. (15).

This result is consistent with the known fact [1, 2] that a 2D flexural phonon propagating in a free-standing slab is characterized by the same atomic displacement pattern as a transverse strain gradient.

4 Computational parameters

Norm-conserving pseudopotentials are generated with Hamann's approach [6], by using the "stringent" parameters of PseudoDojo [7], but neglecting non-linear core corrections. We set a supercell size of $L = 30$ bohr (15.875 Å) and a plane-wave cutoff of 80 Ha; the Brillouin zone is sampled by a Γ-centered 12×12×2 mesh except for silicene (a grid of 13×13×2 points is used); with respect to these parameters, the calculated flexocoefficients are converged within a tolerance of 0.1 % or better (see e.g. Fig. 1). Before performing the linear-response calculations, we optimize the atomic positions and cell parameters of the unperturbed systems to a stringent tolerance (10^{-7} and 10^{-5} atomic units for residual stress and forces,

	a (Å)	b (Å)	h(Å)
Si	3.814	3.814	0.215
(blue) P	3.212	3.212	0.619
BN	2.474	2.474	1.625
SnS_2	3.618	3.618	1.468
RhI_3	6.671	6.671	1.488

Table 1: Equilibrium structural parameters for the unperturbed flat configuration of the materials considered in this work. h corresponds to half the thickness of the buckled materials.

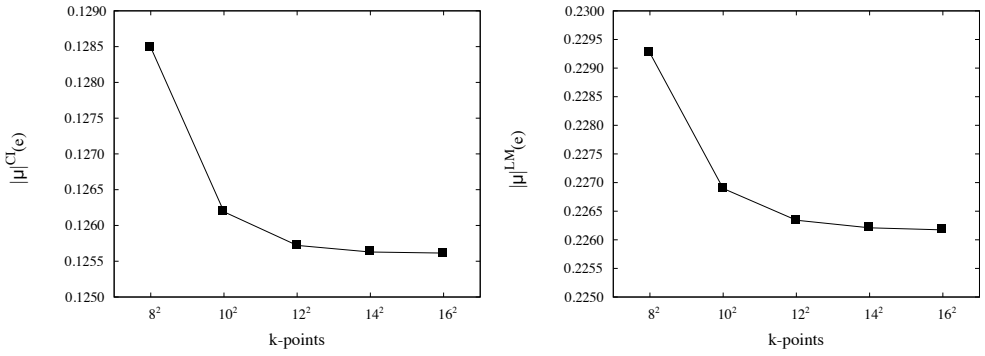

Figure 1: Convergence of the CI (a) and LM (b) independent component $|\mu|$ discussed in the main text as a function of the in-plane **k**-points mesh resolution, for SnS_2.

respectively); the resulting structures (detailed in Tab. 1) are in excellent agreement with existing literature data (see e.g. Ref. [8] and references therein). In particular, for all the materials considered we used an hexagonal unit-cell described by primitve vectors of the form

$$\begin{aligned} \mathbf{a}_1 &= a\ (1.0 \quad, 0.0 \quad, 0.0) \\ \mathbf{a}_2 &= b\ (-0.5 \quad, \sqrt{3}/2 \quad, 0.0) \\ \mathbf{a}_3 &= c\ (0.0 \quad, 0.0 \quad, 1.0) \end{aligned} \tag{21}$$

with $a = b$ (see Table 1) and $c = L$. The atomic structures of the materials studied in this work are provided in Table 2. In the case of RhI_3, after having performed the computation with the structure described in Table 2, we applied a counterclockwise rotation of $\pi/2$ to the calculated flexoelectric tensor, in order to recover the geometry shown in Fig. 2(e) of the main text.

	τ_1	τ_2	τ_3
Si_1	1/3	2/3	$+h_{Si}/L$
Si_2	2/3	1/3	$-h_{Si}/L$
P_1	1/3	2/3	$+h_{P}/L$
P_2	2/3	1/3	$-h_{P}/L$
B_1	1/3	2/3	$+h_{B}/L$
B_2	2/3	1/3	$-h_{B}/L$
N_1	2/3	1/3	$+h_{N}/L$
N_2	1/3	2/3	$-h_{N}/L$
Sn	0	0	0
S_1	1/3	2/3	$+h_{SnS_2}/L$
S_2	2/3	1/3	$-h_{SnS_2}/L$
Rh_1	1/6	5/6	0
Rh_2	5/6	1/6	0
I_1	0.148	0.5	$-h_{RhI_3}/L$
I_2	0.5	0.852	$+h_{RhI_3}/L$
I_3	0.852	0.852	$-h_{RhI_3}/L$
I_4	0.148	0.148	$+h_{RhI_3}/L$
I_5	0.5	0.148	$-h_{RhI_3}/L$
I_6	0.852	0.5	$+h_{RhI_3}/L$

Table 2: Primitive-cell atomic structures, expressed in reduced coordinates, for the materials considered in this work. h refers to the parameter reported in Table.1, except for BN-bilayer where B and N occupy sublattices positions described by slightly different z-components ($h_B = 3.0661$ Bohr and $h_N = 3.0703$ Bohr for B and N respectively).

5 Spontaneous axial polarization in nanotube structures

To test Eq. (9) of the main text, we perform direct ground-state DFT calculations of zigzag SnS_2 nanotubes and extract the atomic forces, together with the macroscopic electronic polarization along the axial direction via the Berry phase implementation of VASP.5.4 [9, 10, 11, 12]. We also perform a full structural relaxation of the nanotube structures to assess the LM contribution to μ, and hence to Eq. (9) of the main text.

Each SnS_2 nanotube is placed in a simulation supercell that is hexagonal over the radial plane, with sufficient outer vacuum regions for the periodic replicas to be mechanically decoupled, and the tube axis is oriented along the z Cartesian direction (with a lattice parameter $c = 11.84$ bohr). We use the projector-augmented wave (PAW) approach with an energy cutoff of 520 eV, the local-density approximation (LDA) to the exchange and correlation potential, and we sample the first Brillouin zone with a grid of $1 \times 1 \times 10$ $\mathbf{k}$ points centered at Γ. The atomic positions are relaxed until all the forces are smaller in magnitude than 2×10^{-4} eV/Å.

In table 3 we show the results obtained for two nanotubes generated by folding stripes of 24 and 36 SnS_2 6-atom unit cells. The CI electronic polarization and the atomic forces are in essentially perfect agreement with the linear-response values shown in the bottom row of the table. Such a match is remarkable given the substantial differences in methods and codes between the two calculations. The atomic relaxations show a slightly slower degree of convergence, which we ascribe to the frequency hardening of the contributing polar phonon with curvature (and therefore a physical effect, not a limitation of our method). Note the two orders of magnitude difference between the axial polarization of our SnS_2 nanotubes and the values reported for a bundle of very thin (< 7.5 bohr radius) h-BN nanotubes. [13]

R	$R \cdot F_z^{\mathrm{Sn}}$	$R \cdot F_z^{\mathrm{S}}$	$P^{\mathrm{1D,CI}}$	$P^{\mathrm{1D,LM}}$
26.122	-0.135	0.066	-0.800	1.106
39.183	-0.130	0.066	-0.789	1.304
l.r.	-0.132	0.065	-0.790	1.422

Table 3: Results from direct calculations for nanotubes of two different radii R [in bohr] (two top rows) and from the linear-response calculation (bottom row). The two left-most columns show the average axial forces [times R and in hartree units] on the Sn and S atoms. The two right-most columns show the clamped-ion and lattice-mediated 1D axial nanotube polarizations [in e]. Direct 1D polarizations are calculated as $\Omega P_z/c$, with Ω, c and P_z being, respectively, the volume, dimension and 3D polarization component along the axial direction of the simulation supercell. In turn, linear response ones are calculated with Eq. (9) of the main text.

6 Longitudinal electric fields induced by a flexural phonon

Let us consider a flexural phonon traveling in a suspended quasi-2D crystal with a small in-plane momentum $\mathbf{q} = (q_x, q_y, 0)$. In the first-order linear regime, the displacement pattern of such a mode can be written as a cell-periodic part times a phase as follows

$$u^l_{\kappa\beta} = u^{\mathbf{q}}_{\kappa\beta} e^{\mathbf{q}\cdot\mathbf{R}_{l\kappa}} = U\left(\delta_{\beta z} - iq_\beta \tau_{\kappa z}\right) e^{\mathbf{q}\cdot\mathbf{R}_{l\kappa}}, \tag{22}$$

where $\mathbf{R}_{l\kappa}$ is the position of the atom κ in the cell l, and we have performed a long-wavelength expansion of the cell-periodic part up to first order in the momentum (see e.g. Sec. 2.2 of the Supplemental Material of Ref. [1]).

We shall show here that the lattice distortion given by Eq. (22) induces long-range electrostatic fields along the longitudinal (in-plane) direction. To this end, we resort to the formalism developed in Refs. [14, 15, 16], where the in-plane electrostatic potential generated by a charge perturbation is expressed as

$$V^{\parallel}(\mathbf{q}) = 2\pi \frac{\rho^{\parallel}(\mathbf{q})}{q}, \tag{23}$$

with $q = |\mathbf{q}|$. The $\parallel$ superscript equivalently means that both the potential and charge density are even functions with respect to a reflection along the out-of-plane direction. The charge response to the perturbation parameter U is built from the individual sublattices displacements as follows

$$\rho^{\parallel}(\mathbf{q}) = \sum_{\kappa\beta} \left(\delta_{\beta z} - iq_\beta \tau_{\kappa z}\right) \rho^{\parallel}_{\kappa\beta}(\mathbf{q}), \tag{24}$$

with

$$\rho^{\parallel}_{\kappa\beta}(\mathbf{q}) = \int dz \rho^{\mathbf{q}}_{\kappa\beta}(z)\, \cosh(qz), \tag{25}$$

and $\rho^{\mathbf{q}}_{\kappa\beta}(z)$ being the in-plane average of the microscopic charge-density response to the displacement of atom κ along β.

Our goal is to derive a practical formulation of Eq. (23) by pursuing the usual long-wavelength expansion of the constituent objects. This procedure requires to combine Eq. (22) with

$$\cosh(qz) = 1 + \frac{q^2 z^2}{2} + \cdots, \tag{26}$$

and with the long-wavelength expansion of the microscopic charge-density respsonse

$$\rho^{\mathbf{q}}_{\kappa\beta}(z) = \rho_{\kappa\beta}(z) - iq_\gamma \rho^{(1,\gamma)}_{\kappa\beta}(z) - \frac{q_\gamma q_\delta}{2} \rho^{(2,\gamma\delta)}_{\kappa\beta}(z) + i\frac{q_\gamma q_\delta q_\lambda}{6} \rho^{(3,\gamma\delta\lambda)}_{\kappa\beta}(z) \cdots \tag{27}$$

to arrive at a corresponding expansion for $\rho^{\parallel}(\mathbf{q})$. At zero-th and first order in $\mathbf{q}$, $\rho^{\parallel}(\mathbf{q})$ vanishes because of the acoustic sum rule and charge neutrality; at second order it also vanishes

because of rotational invariance. We therefore focus on the leading $O(q^3)$ contributions to $\rho^{\parallel}(\mathbf{q})$,

$$\begin{aligned}\rho^{\parallel}(\mathbf{q}) =& -i\frac{q^2 q_\beta}{2}\sum_\kappa\left[\int dz\, z^2 \rho_{\kappa z}^{(1,\beta)}(z) + \tau_{\kappa z}\int dz\, z^2 \rho_{\kappa\beta}(z)\right] \\ &+ i\frac{q_\beta q_\delta q_\lambda}{6}\sum_\kappa\left[\int dz\, \rho_{\kappa z}^{(3,\beta\delta\lambda)}(z) + 3\tau_{\kappa z}\int dz\, \rho_{\kappa\beta}^{(2,\delta\lambda)}(z)\right] + O(q^4).\end{aligned} \tag{28}$$

The first line on the rhs vanishes identically. To prove this, we use the following relations [4],

$$\sum_\kappa \rho_{\kappa z}^{(1,\gamma)}(\mathbf{r}) = \sum_\kappa \rho_{\kappa\gamma}^{(1,z)}(\mathbf{r}) = \sum_\kappa (z-\tau_{\kappa z})\rho_{\kappa\gamma}(\mathbf{r}). \tag{29}$$

Then the sublattice sum of the first square bracket reduces to

$$\int dz\, z^3 \sum_\kappa \rho_{\kappa\gamma}(z) = -\frac{1}{S}\int d^3r\, z^3 \frac{\partial\rho(\mathbf{r})}{\partial r_\gamma} \tag{30}$$

(where translational invariance has been used in the last equality and $\rho(\mathbf{r})$ corresponds the microscopic charge density within the undistorted configuration), which is manifestly zero after integration by parts (recall that γ here refers to an in-plane direction). In the end, we reach a simpler final expression that can be written as follows (summation over repeated indices is implied)

$$\rho^{\parallel}(\mathbf{q}) = iq_\alpha q_\beta q_\gamma\left(\frac{1}{6S}\sum_\kappa O_{\kappa z}^{(\alpha\beta\gamma)} + \frac{1}{2S}\sum_\kappa \tau_{\kappa z} Q_{\kappa\alpha}^{(\beta\gamma)}\right), \tag{31}$$

where S is the in-plane area of the primitive cell while $\mathbf{Q}$ and $\mathbf{O}$ are, respectively the 3D dynamic quadrupole and octupole tensors of the supercell. This result can be further simplified after recalling the following relations between charge density and polarization moments [4]

$$\frac{1}{2}\sum_k O_{\kappa z}^{(\alpha\beta\gamma)} = \Omega\left(\bar{\mu}^{\mathrm{I}}_{\alpha z,\beta\gamma} + \bar{\mu}^{\mathrm{I}}_{\beta z,\gamma\alpha} + \bar{\mu}^{\mathrm{I}}_{\gamma z,\alpha\beta}\right), \tag{32}$$

$$Q_{\kappa\gamma}^{(\alpha\beta)} = \Omega\left(\bar{P}^{(1,\beta)}_{\alpha,\kappa\gamma} + \bar{P}^{(1,\alpha)}_{\beta,\kappa\gamma}\right). \tag{33}$$

After gathering all terms in Eq.(31) (and using the relation $\Gamma^\kappa_{\alpha,z\beta} = \Gamma^\kappa_{\alpha,\beta z} = -\delta_{\alpha\beta}\tau_{\kappa z}$ valid for an isolated slab), we find

$$\rho^{\parallel}(\mathbf{q}) = iq_\alpha q_\beta q_\gamma \frac{L}{3}\left(\mu^{\mathrm{I,el}}_{\alpha z,\beta\gamma} + \mu^{\mathrm{I,el}}_{\beta z,\gamma\alpha} + \mu^{\mathrm{I,el}}_{\gamma z,\alpha\beta}\right) + O(q^4) \tag{34}$$

Recalling the relation proved in section 3.3

$$\mu^{\mathrm{2D,CI}}_{\alpha z,\beta\gamma} = -L\mu^{\mathrm{I,el}}_{\alpha z,\beta\gamma} \tag{35}$$

we arrive at

$$\rho^{\parallel}(\mathbf{q}) = -iq_\alpha q_\beta q_\gamma \mu^{\mathrm{2D,CI}}_{\alpha z,\beta\gamma} + O(q^4). \tag{36}$$

This result, which can be trivially generalized to the relaxed-ion case, in combination with Eq. (23) yields Eq. (10) of the main text.

Note that, in the flexural phonon considered in this Section, the symmetrized strain-gradient tensor reads as

$$\varepsilon_{\beta\gamma,z}(\mathbf{r}) = U q_\beta q_\gamma e^{i\mathbf{q}\cdot\mathbf{r}}, \tag{37}$$

and via Eq. (2) of the main text yields a flexoelectric polarization

$$\frac{\partial P_\alpha(\mathbf{r})}{\partial U} = q_\beta q_\gamma \mu^{\mathrm{2D,CI}}_{\alpha z,\beta\gamma} e^{i\mathbf{q}\cdot\mathbf{r}}. \tag{38}$$

By applying $\rho = -\nabla\cdot\mathbf{P}$, we trivially recover Eq. (36), proving the consistency of our definition of $\boldsymbol{\mu}^{\mathrm{2D}}$ with the fundamental treatment of electrostatics in 2D developed in Ref. [14].

7 Choice of the exchange-correlation functional

To verify the impact of the exchange-correlation functional, we recalculated the flexoelectric coefficient μ^{2D} defined in the main text by using the PBE functional in place of LDA; the results are presented in Table 4. The LDA and PBE results show reasonable agreement in most cases, with typical deviations that are in line with the expectations (e.g., similar deviations were pointed out for the out-of-plane response in our earlier work [1]). The largest disagreement occurs in the case of the BN bilayer, with a PBE flexoelectric coefficient that is 35% larger than the LDA value. Interestingly, a closer look at the relaxed PBE

	$\mu^{\mathrm{2D}}_{yz,xx}$			$\mu^{\mathrm{2D}}_{zz,xx}$
	CI	LM	RI	RI
Si	0.0239	0.0000	0.0239	0.0016
P	0.0669	0.0000	0.0669	0.0206
SnS_2	0.1369	−0.2016	−0.0646	0.0178
RhI_3	−0.1733	0.0202	−0.1530	−0.0080
2-BN (direct)	1.0013	−0.6215	0.3797	−0.0254
2-BN (model)	0.9986	−0.6213	0.3773	

Table 4: Calculated 2D flexoelectric coefficients within PBE. Left columns show the Clamped-Ion(CI), Lattice-Mediated(LM), and Relaxed-Ion(RI) contributions to the in-plane response $\mu^{\mathrm{2D}}_{yz,xx}$. The right column shows the out-of-plane RI response, $\mu^{\mathrm{2D}}_{zz,xx}$. Results are provided in units of electronic charge. 2-BN corresponds to the BN bilayer, which we calculated either directly or by means of the piezoelectric model ($\mu^{\mathrm{2D}} = Eh$) within PBE. The values of the CI and LM longitudinal piezoelectric constant are $E^{\mathrm{CI}} = 0.1208$ e/bohr and $E^{\mathrm{LM}} = -0.0749$ e/bohr, respectively, in good agreement with the LDA values reported in the main text. The calculated PBE interlayer distance is $h = 8.29$ bohr.

structure reveals that the equilibrium interlayer distance, $h_{\mathrm{PBE}} = 8.29$ bohr, displays a comparable (35%) overestimation respect to the LDA result ($h_{\mathrm{LDA}} = 6.14$ bohr). Given that the noninteracting-layer formula, $\mu = Eh$, accurately holds in both cases (compare the "direct" and "model" row in Table 4), the large disagreement in the interlayer distance h is almost entirely responsible for the discrepancy in the calculated μ. (The piezoelectric coefficient of monolayer BN, E, has similar values in LDA and PBE.)

Such a discrepancy in the value of h is not surprising, and arises from the fact that a bilayer system is a van der Waals bonded compound, i.e., a classic situation where local and semilocal approximations to DFT fail. PBE, in particular, does not seem to bind the two BN layers at all, which explains the unusually large value of h. This structural parameter has been calculated by taking van der Waals corrections into account, at various levels of theory, in [17]. The most reliable values quoted therein, of $h = 3.34 - 3.51$ Å, are similar (3–9% larger) to our LDA value, and 20% smaller than the PBE one. All in all, this analysis indicates that whenever the vdW corrections are needed, the flexoelectric response of the system is trivially given as a weighted sum of the piezoelectric response of the constituents, in agreement with the conclusions of [18].

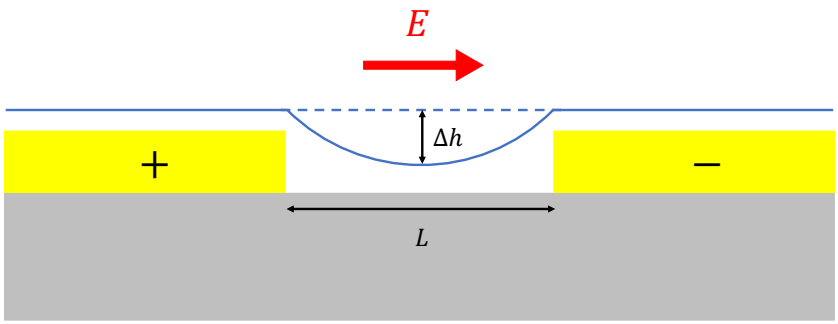

Figure 2: Schematic representation of the experimental setup proposed. The layer is deposited above two electrodes separated by a distance L and in turns leaned on a substrate. The two electrodes are used to apply an in-plane uniform electric field E inducing a curvature of the layer in corrispondence with the hole, where the layer is allowed to deform.

8 Experimental setup

In this section we propose two possible experimental setups that could be used to confirm our theoretical predictions.

8.1 External electric field-induced bending

Let us consider the system schematically illustrated in Fig.2. It consists of a single layer (blue) deposited on a gap between two metallic electrodes (yellow), both lying on a flat substrate (grey). The system can be regarded as extended along the normal direction (not shown). Depositing 2D layers on nanopatterned substrates with gaps of various shapes and dimensions is a well established experimental practice, see e.g. Ref. [19], so the setup of Fig.2 should be reasonably straightforward to prepare.

By applying an alternating in-plane electric field, our theory predicts that the layer-membrane will start to vibrate vertically at the same frequency, at an amplitude that depends on the crystallographic orientation of the layer. In particular, the response should be largest when one of the mirror planes of the crystal is parallel to the direction of the electric field, and vanish if one of such planes is perpendicular to it. By probing the system near the electromechanical resonance (within the linear regime, the suspended layer can be accurately modeled as a damped harmonic oscillator [19]), a detectable feature should appear in the measured capacitance. The amplitude of such signal, together with the relevant mechanical and geometrical parameters of the system, should provide a reliable quantitative estimatimate of the flexoelectric coefficient that we define and calculate in this work.

As an alternative, one could also probe the vertical displacements of the layer directly, e.g., via an AFM tip. In such case, the electromechanical response of the system might be complicated by the coupling to the tip, but the most important qualitative signatures of the effect (e.g. its directional dependence) should be detectable nonetheless.

8.2 Second harmonic generation method

The second experimental setup builds on the use of the Second Harmonic Generation (SHG) technique. As we illustrate in the main text, rippled and bent geometries are decorated with topologically nontrivial polarization textures via the physical effect we discuss here. SHG is sensitive to a local breakdown of space inversion (SI) symmetry and on the direction along which SI is broken; it could be used, therefore, to detect the predicted polarization patterns. The use of SHG in 2D systems is well documented (see, e.g., [20]) and could, in principle, be applicable to characterizing the effects that we describe.

As a means to obtain the desired ripple patterns, one could again use nanopatterning techniques, as explained in the above paragraphs. Indeed, suspended layers are seldom flat: they typically feel the van der Waals attraction of the far-away substrate and tend to bend inward. This means that an in-plane polarization should be present in a suspended layer, with a topology that depends on the shape of the gap, even in absence of an applied electric field.

9 Topological polarization textures in arbitrary rippled structures

For a generic ripple $u_z(x,y)$, at the first order in the local shape-operator tensor field $b_{\beta\gamma}(x,y)$, the induced 2D local polarization vector field can be written as

$$P^{2D}_{\alpha}(x,y) = \mu^{2D}_{\alpha z,\beta\gamma} b_{\beta\gamma}(x,y), \tag{39}$$

with β,γ referring to in-plane directions while $\alpha = x,y,z$. μ^{2D} is the 2D flexoelectric coefficient as defined in the main text, for $\alpha = x,y$, and as $\mu^{2D} = \epsilon_0\varphi$, for $\alpha = z$ [1]. Sum over repeated indices is understood. In turn, the local shape-operator tensor field is given by

$$b_{\beta\gamma}(x,y) = \frac{\partial^2 u_z(x,y)}{\partial r_\beta r_\gamma}. \tag{40}$$

Within the symmetries of the materials considered, we have

$$\begin{aligned} P^{2D}_x(x,y) &= 2\mu^{2D} b_{xy}(x,y), \\ P^{2D}_y(x,y) &= \mu^{2D}\left(b_{xx}(x,y) - b_{yy}(x,y)\right), \\ P^{2D}_z(x,y) &= \epsilon_0\varphi Tr(b), \end{aligned} \tag{41}$$

where $Tr(b) = \sum_\beta b_{\beta\beta}(x,y)$ is the trace of the local shape-operator field.

In Fig.3 and 4 we report the resulting in-plane polarization field associated to several types of ripples, within the kind of materials considered in the main text.

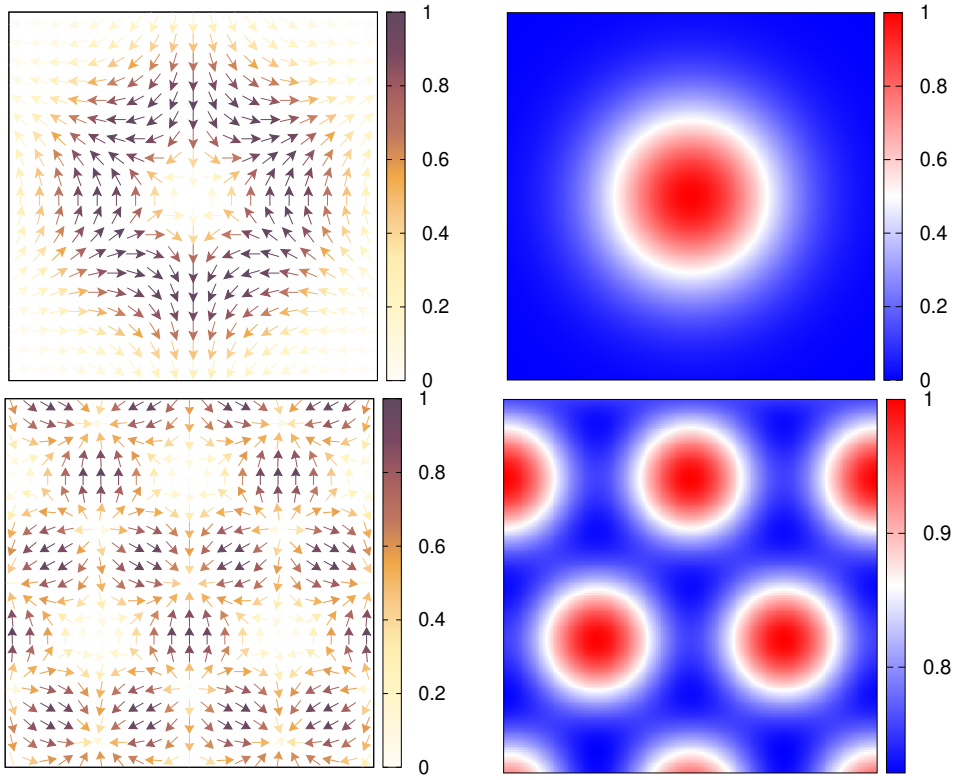

Figure 3: Top and bottom left panels: Polarization texture associated with a single Gaussian bump of the type $z = Ae^{-(x^2+y^2)/\sigma^2}$ and an hexagonal lattice of Gaussian bumps of the same type. The arrows indicate the polarization direction, its amplitude (in units of $|P_{\|}|^{\max} \simeq 1.48\frac{A\mu}{\sigma^2}$ and $|P_{\|}|^{\max} \simeq 6.94\frac{A\mu}{\sigma^2}$ rispectively) is defined by the color scale. Top and bottom right panels: Contour plot for the considered deformation. Their amplitudes (in units of $u_z^{\max} = A$ and $u_z^{\max} \simeq 1.11A$ respectively) are defined by the color scale.

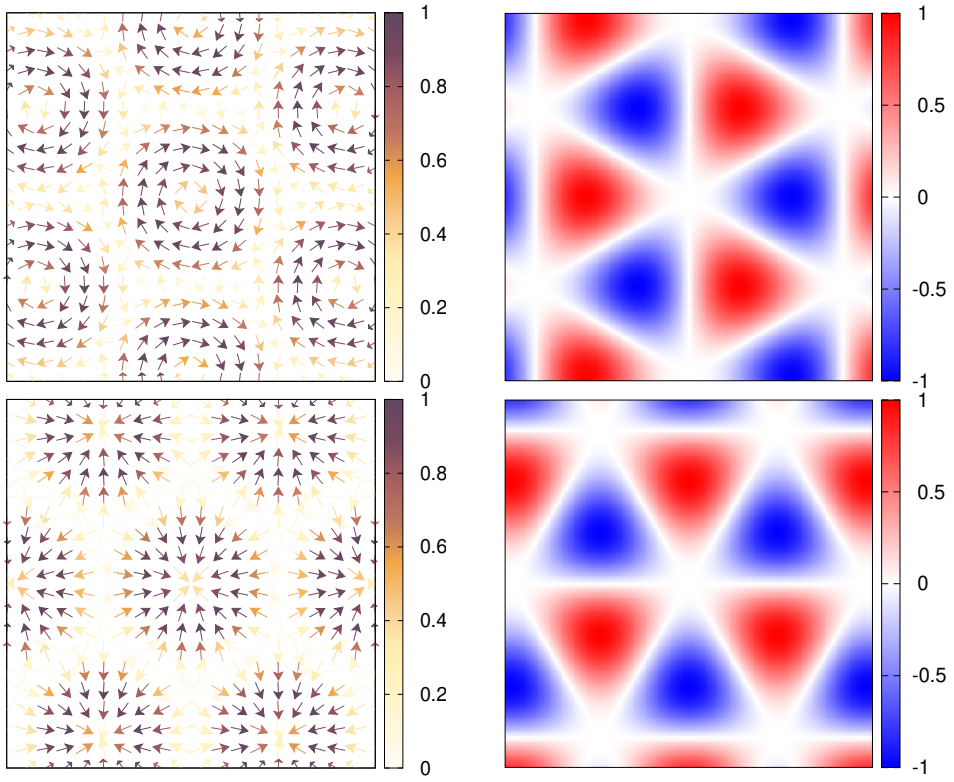

Figure 4: Top and bottom left panels: Polarization texture associated with two periodic patterns of the type $z = A\sum_{i=1}^{3}\sin(\mathbf{q_i}\cdot\mathbf{r})$, with $\mathbf{q}_1 = q(1,0,0)$, $\mathbf{q}_2 = q(-1/2,\sqrt{3}/2,0)$, $\mathbf{q}_3 = q(-1/2,-\sqrt{3}/2,0)$, and $\mathbf{q}_1 = q(\sqrt{3}/2,1/2,0)$, $\mathbf{q}_2 = q(-\sqrt{3}/2,1/2,0)$, $\mathbf{q}_3 = q(0,-1,0)$ respectively. $q = 2\pi/L$. The arrows indicate the polarization direction, its amplitude (in units of $|P_{\|}|^{\max} = 1.75A\mu q^2$) is defined by the color scale. Top and bottom right panels: Contour plot of the periodic deformations considered. Their amplitudes (in units of $u_z^{\max} \simeq 2.6A$) are defined by the color scale.

References

[1] M. Springolo, M. Royo and M. Stengel. *Direct and converse flexoelectricity in two-dimensional materials.* Phys. Rev. Lett., **127**, 216801 (2021).

[2] M. Stengel. *Microscopic response to inhomogeneous deformations in curvilinear coordinates.* Nature Communications, **4**, 2693 (2013).

[3] M. Stengel and D. Vanderbilt. *First-principles theory of flexoelectricity.* A. K. Tagantsev and P. V. Yudin (editors), *Flexoelectricity in Solids From Theory to Applications*, chapter 2, 31–110. World Scientific Publishing Co., Singapore (2016).

[4] M. Stengel. *Flexoelectricity from density-functional perturbation theory.* Phys. Rev. B, **88**, 174106 (2013).

[5] M. Royo and M. Stengel. *Lattice-mediated bulk flexoelectricity from first principles.* Phys. Rev. B, **105**, 064101 (2022).

[6] D. R. Hamann. *Optimized norm-conserving Vanderbilt pseudopotentials.* Phys. Rev. B, **88**, 085117 (2013).

[7] M. van Setten, M. Giantomassi, E. Bousquet, M. Verstraete, D. Hamann, X. Gonze and G.-M. Rignanese. *The PseudoDojo: Training and grading a 85 element optimized norm-conserving pseudopotential table.* Comp. Phys. Comm., **226**, 39 (2018).

[8] K. Novoselov, A. Mishchenko, A. Carvalho and A. Castro Neto. *2D materials and van der Waals heterostructures.* Science, **353**, aac9439 (2016).

[9] G. Kresse and J. Hafner. *Ab initio molecular dynamics for liquid metals.* Phys. Rev. B, **47**, 558 (1993).

[10] G. Kresse and J. Hafner. *Ab initio molecular-dynamics simulation of the liquid-metal–amorphous-semiconductor transition in germanium.* Phys. Rev. B, **49**, 14251 (1994).

[11] G. Kresse and J. Furthmüller. *Efficiency of ab-initio total energy calculations for metals and semiconductors using a plane-wave basis set.* Computational Materials Science, **6**, 15 (1996).

[12] G. Kresse and D. Joubert. *From ultrasoft pseudopotentials to the projector augmented-wave method.* Phys. Rev. B, **59**, 1758 (1999).

[13] S. M. Nakhmanson, A. Calzolari, V. Meunier, J. Bernholc and M. B. Nardelli. *Spontaneous polarization and piezoelectricity in boron nitride nanotubes.* Physical Review B, **67**, 235406 (2003).

[14] M. Royo and M. Stengel. *Exact Long-Range Dielectric Screening and Interatomic Force Constants in Quasi-Two-Dimensional Crystals.* Phys. Rev. X, **11** (2021).

[15] S. Poncé, M. Royo, M. Gibertini, N. Marzari and M. Stengel. *Accurate Prediction of Hall Mobilities in Two-Dimensional Materials through Gauge-Covariant Quadrupolar Contributions.* Phys. Rev. Lett., **130**, 166301 (2023).

[16] S. Poncé, M. Royo, M. Stengel, N. Marzari and M. Gibertini. *Long-range electrostatic contribution to electron-phonon couplings and mobilities of two-dimensional and bulk materials*. Phys. Rev. B, **107**, 155424 (2023).

[17] S. Zhou, J. Han, S. Dai, J. Sun and D. J. Srolovitz. *van der Waals bilayer energetics: Generalized stacking-fault energy of graphene, boron nitride, and graphene/boron nitride bilayers*. Phys. Rev. B, **92**, 155438 (2015).

[18] K.-A. N. Duerloo and E. J. Reed. *Flexural electromechanical coupling: a nanoscale emergent property of boron nitride bilayers*. Nano letters, **13**, 1681 (2013).

[19] P. G. Steeneken, R. J. Dolleman, D. Davidovikj, F. Alijani and H. S. J. van der Zant. *Dynamics of 2D material membranes*. 2D Materials, **8**, 042001 (2021).

[20] J. Zhang, W. Zhao, P. Yu, G. Yang and Z. Liu. *Second harmonic generation in 2D layered materials*. 2D Materials, **7**, 042002 (2020).